

# Towards Calibration-Free Imaging through Dense, Volumetric Scattering with Differential Diffusion Approximation Model

Tomohiro Maeda<sup>1,\*</sup>, Ankit Ranjan<sup>2</sup>, and Ramesh Raskar<sup>1</sup>

<sup>1</sup>Media Lab, Massachusetts Institute of Technology, Cambridge, MA 02139

<sup>2</sup>Nuffield Department of Surgical Sciences, University of Oxford, Oxford OX3 9DU, UK

\*tomotomo@mit.edu

## ABSTRACT

Imaging through dense scattering media — such as biological tissue, fog, and smoke — has significant applications in the medical and robotics fields. We propose a novel framework for imaging through homogeneous scattering media with unknown optical properties for non-invasive sensing and diagnostics. The proposed technique exploits time-of-flight measurement and an auto-differential forward model to estimate both the optical properties of the scattering media and a target within the media. Our approach achieves practical and non-invasive imaging through turbid media with a simple optical setup, without requiring tedious calibrations to acquire the sensor position or optical properties of the media.

## Introduction

The ability to image through dense, volumetric scattering media has many potential applications in the biomedical and robotics fields, such as non-invasive diagnostics and autonomous navigation through a fog. There are many technical challenges in imaging through scattering media, which various works have attempted to solve.

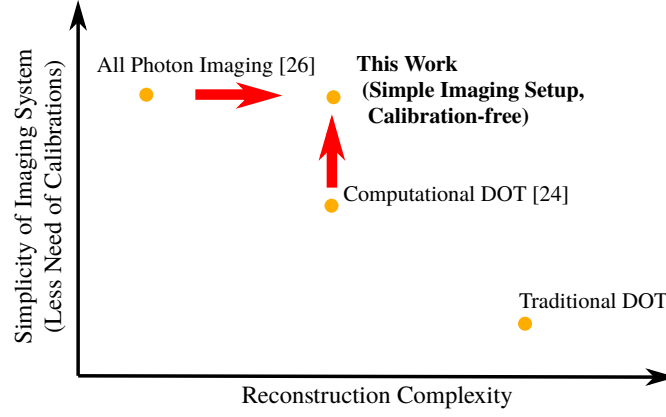
Optical coherence tomography<sup>1</sup>, confocal microscopy<sup>2</sup>, and two-photon imaging<sup>3</sup> optically gate ballistic photons to see thorough thin scattering media with high resolution. These techniques achieve cellular-scale resolution, but do not image deep in the tissue. Time-of-flight measurement enables time-gating of ballistic photons to see through scattering media<sup>4–6</sup>. The separation of ballistic from scattered photons is also used at larger scales for computer vision and robotics<sup>7–9</sup>. However, techniques which image with ballistic photons suffer from a low signal-to-noise ratio (SNR), because the number of ballistic photons decreases in deeper tissue. Speckle-based techniques<sup>10,11</sup> achieve refraction-limited resolution through scattering media, but their application is limited by a small field-of-view due to the memory effect<sup>12</sup>. Speckle can also be modeled as a sum of complex field to construct complex-valued linear system, which can be inverted to reconstruct an image through scattering<sup>13,14</sup>, but capturing this linear system requires tedious calibrations with fixed target and media.

Photo-acoustic tomography (PAT)<sup>15–17</sup> and diffuse optical tomography (DOT)<sup>18,19</sup> are often used for imaging through deep, dense scattering media. PAT combines optics and ultrasound to benefit from both high optical contrast and the negligible scattering of ultrasound. DOT models the propagation of the diffused photons that undergo a significant number of scatterings, and reconstructs the optical properties such as scattering coefficient and absorption coefficient<sup>20</sup>.

Recently, the computational techniques to exploit time-of-flight information have been developed for novel imaging such as non-line-of-sight imaging<sup>21</sup>, imaging through fog<sup>22</sup>, transient imaging<sup>23</sup>, time-folded optics<sup>24</sup>. Time-of-flight measurement are also exploited for DOT<sup>25–27</sup>. Gkioulekas et al. showed that the ability to resolve pathlength of photons is beneficial for reconstructing a complex, scattering volume<sup>28</sup>. In this work, we exploit time-of-flight measurement for the estimation of the optical properties.

Similarly to DOT, we exploit the diffusion approximation to model light transport. However, in contrast to DOT, the goal of this work is to develop a framework to reconstruct objects in scattering media with a simple imaging setup that does not need extensive calibration. Specifically, our contribution is the auto-differential diffusion approximation model to recover both optical properties and the object shape. We demonstrate a recovery of a target with a single-shot measurement with a short acquisition time, which shows the potential to real-time imaging through highly scattering media.

**Relation to prior art:** All Photon Imaging (API)<sup>29</sup> is the most related process to our work. Similar to API, our method does not require prior knowledge of the optical properties of the medium and is capable of recovering the target from a single-shot measurement. API considers a scene where the direct illumination of the target is possible. In contrast, we consider more complex scenes, where the target is not directly accessible from the illumination source. In this paper, we incorporate a forward



**Figure 1. Towards imaging more complex scene with simple imaging system.** Our technique exploits auto-differential diffusion approximation to simultaneously recover the target and the optical properties of the scattering media.

model that is differentiated with respect to the optical properties. This framework enables calibration-free measurements, as there is no need for prior measurements for the estimation of the unknown optical properties. Fig. 1 illustrates the motivation of this work.

## Results

### Forward Model

The radiative transfer function (RTE) describes the random walk of photons through a homogeneous medium as follows:

$$\frac{1}{c} \frac{\partial L(\mathbf{r}, \omega, t)}{\partial t} + \omega \cdot \nabla L(\mathbf{r}, \omega, t) = -\mu_t L(\mathbf{r}, \omega, t) + \mu_s \int L(\mathbf{r}, \omega, t) P(\omega, \omega') d\Omega' + S(\mathbf{r}, \omega, t), \quad (1)$$

where the left two terms represent the change of the energy (per unit volume per unit solid angle) and the divergence of the beam, while the right three terms represent the extinction, scattered energy from the surrounding, and light source.  $\mu_a$  and  $\mu_s$  respectively represent the expected number of absorption and scattering per unit light path, and  $\mu_t$  is a sum of  $\mu_a$  and  $\mu_s$ .  $\mathbf{r}, \omega, t$  denote the location, direction and time.  $c$  is a speed of light in the media.  $L(\mathbf{r}, \omega, t), P(\omega, \omega')$  denote the radiance and phase function respectively. The phase function is often represented by the anisotropy parameter  $g = \langle \cos \theta \rangle$ , where  $\theta$  is the angle between the old and new trajectories.

The RTE is hard to solve, so two approaches are often used for approximations. When the number of scattering events is sufficiently large and  $\mu_a \ll \mu_s$ , the diffusion equation approximates the RTE, where the photon fluence rate  $\phi(\mathbf{r}, t) = \int L(\mathbf{r}, \omega, t) d\Omega$  satisfies the diffusion equation. The diffusion approximation becomes less accurate as the number of scatterings becomes small, and the propagation of photons cannot be considered diffusion. In situations with limited scattering, a Monte Carlo approximation is used to approximate the RTE. However, Monte Carlo approximations are computationally expensive as they involve the simulation of the random walks of millions of photons.

We consider dense and thick scattering media, where the diffusion approximation can provide a reasonably accurate solution to the RTE. The diffusion equation is written as

$$\frac{1}{c} \frac{\partial}{\partial t} \phi(\mathbf{r}, t) - D \nabla^2 \phi(\mathbf{r}, t) + \mu_a \phi(\mathbf{r}, t) = S(\mathbf{r}, t), \quad (2)$$

where  $D = [3(\mu_a + \mu_s(1 - g))]^{-1}$  is the diffusion coefficient. For an isotropic light source with short time pulse, the photon fluence rate in the infinite scattering media is written as

$$\phi(\mathbf{r}, t) = c(4\pi Dct)^{-3/2} \exp\left(-\frac{r^2}{4Dct} - \mu_a ct\right). \quad (3)$$

As illustrated in Fig. 3, our imaging setup is in transmission mode, where a target is between scattering media. Unlike traditional diffuse optical tomography, the goal of our technique is to reconstruction a 2D target within a scattering media with high contrast. We express the measurement as the result of a 3D convolution with  $K_1(x, y, t)$  (scattering between illumination

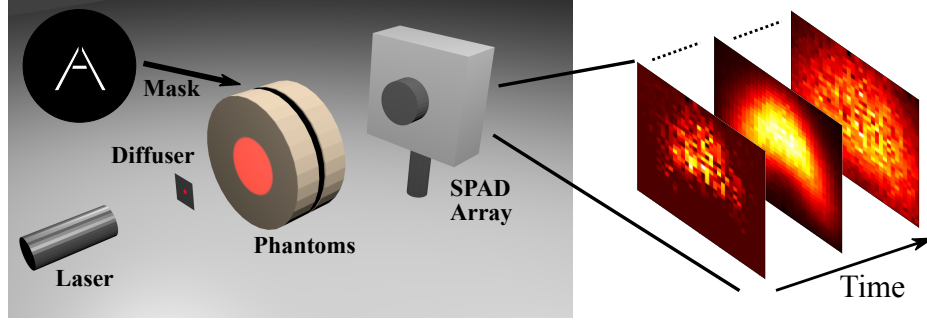


**Figure 2. Imaging system to see through scattering media.** A single-photon avalanche diode (SPAD) array captures 3D measurement. The blurring due to volumetric scattering makes it challenging to see the target directly from the measurement.

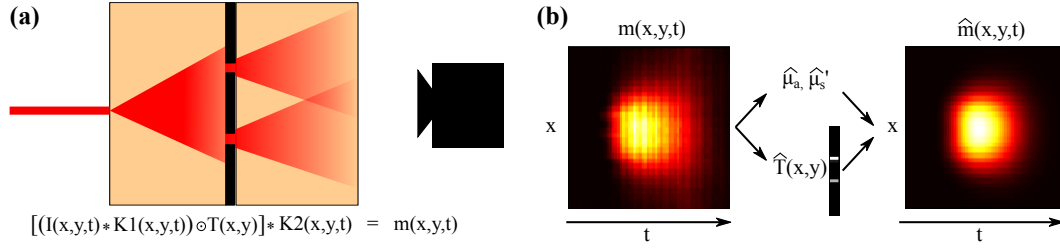


**Figure 3. A sketch of the forward model and reconstruction.** (a) The illumination ( $I(x,y)$ ) is blurred as photons scatter in the first scattering media ( $K_1(x,y,t;D,d_1)$ ) before passing through the 2D target ( $T(x,y)$ ). Photons scatter in the second scattering media ( $K_2(x,y,t;D,d_2)$ ) before reaching the detector. We illustrate the forward model in 2D for simplicity. Our reconstruction method takes the 3D measurement over  $x$ ,  $y$ , and  $t$  for input. (b) Our technique estimates the unknown optical properties of the media by minimizing the observed measurement  $m(x,y,t)$  and estimated measurement ( $\hat{m}(x,y,t)$ ).

and target), followed by a 2D multiplication with  $T(x,y)$  (2D mask) and another 3D convolution with  $K_2(x,y,t)$  (scattering between target and detector):

$$m(x,y,t) = [I(x,y,t) * K_1(x,y,t;D,d_1)] \odot T(x,y) * K_2(x,y,t;D,d_2). \quad (4)$$

$I(x,y,t)$  denotes the illumination on the surface of the scattering media. Our forward model is similar to the model proposed by Lyons et al.<sup>27</sup> We follow diffusion approximation model proposed by Patterson et al.<sup>30</sup> to write the 3D kernel  $K_1(x,y,t;D,d_1)$ ,  $K_2(x,y,t;D,d_2)$  that represent the propagation of photons through the scattering media with thickness  $d$  as follows.

$$K(x,y,t;D,d) = (4\pi Dc)^{-3/2} t^{-5/2} \exp(-\mu_a ct) \exp(-\frac{|r|^2}{4Dct}) \\ \times \left[ (d - z_0) \exp(-\frac{(d - z_0)^2}{4Dct}) - (d + z_0) \exp(-\frac{(d + z_0)^2}{4Dct}) \right. \\ \left. + (3d - z_0) \exp(-\frac{(3d - z_0)^2}{4Dct}) - (3d + z_0) \exp(-\frac{(3d + z_0)^2}{4Dct}) \right], \quad (5)$$

where  $z_0 = [\mu_s(1 - g)]^{-1}$  and  $|r|^2 = x^2 + y^2 + d^2$ . This is different from Eq. 2 because we consider the photon transmittance of a homogeneous slab media that is bounded along optical axis, and infinite in the other two axes. Applying two boundary conditions for surfaces of the slab geometry results in Eq. 5.

### Reconstruction Algorithm

Our method estimates the 2D target as well as the optical properties of the homogeneous scattering media from the measurement. We write the objective of the algorithm as follows.

$$\min_{T(x,y), D} \|m(x,y,t) - [I(x,y,t) * K_1(x,y,t;D,d_1)] \odot T(x,y) * K_2(x,y,t;D,d_2)\|^2 + \Gamma(T(x,y)), \quad (6)$$

---

**Algorithm 1: ADMM algorithm to solve Eq. 11**

---

**Input:** Input:  $\mathbf{v}^0, \mathbf{z}^0 = \text{vec}(\hat{T}(x, y))$ ,  $\mathbf{u}^0 = 0$ ,  $\rho, \lambda_1, \lambda_2$

**while not converged do**

- 1  $\mathbf{v}^{i+1} = (\mathbf{A}^\top \mathbf{A} + \rho \mathbf{G}^\top \mathbf{G})^{-1} (\mathbf{A}^\top \mathbf{b} + \rho \mathbf{z}^i - \mathbf{u}^i).$
  - 2  $\mathbf{z}^{i+1} = \max(|\mathbf{v}^{i+1} - \mathbf{u}^i| - \lambda/\rho, 0).$
  - 3  $\mathbf{u}^{i+1} = \mathbf{u}^i + \mathbf{v}^{i+1} - \mathbf{z}^{i+1}.$
- 

We solve this problem in the model by minimizing with respect to the optical property and the target in an alternate manner.

Scattering coefficient  $\mu_s$ , anisotropy  $g$ , and absorption coefficient  $\mu_a$  are commonly used to represent the scattering properties of media. In the diffusion paradigm, the scattering coefficient and anisotropy are interchangeable, so reduced scattering coefficient  $\mu'_s = \mu_s(1 - g)$  is used instead. While we assume  $\mu_a \ll \mu_s$ ,  $\mu_a$  still has a significant impact on the 3D kernel  $K(x, y, t)$ . Hence, our goal is to estimate  $\mu'_s$  and  $\mu_a$  from the measurement.

**Estimation of  $\mu_a$ :** As Chance et al.<sup>31</sup> suggest, the absorption coefficient  $\mu_a$  can be estimated with the asymptotic slope of the log of the measurement along the time dimension. Let us consider the blur kernel  $K(x, y, t; D, d)$  for large  $t$  (See Supplemental Material for the derivation):

$$\lim_{t \rightarrow \infty} \frac{\partial}{\partial t} \log K(x, y, t; D, d) = \mu_a c. \quad (7)$$

Hence,  $t$  is sufficiently large  $\mu_a$  can be estimated as

$$\hat{\mu}_a \approx -\frac{1}{c} \frac{\partial}{\partial t} \log K(x, y, t = t_l; D, d). \quad (8)$$

Our forward model is more complex than the expression of the 3D kernel in Eq. 5. However, the insight from Eq. 7 shows that the slope of the log of the measurement is dominantly determined by  $\mu_a$ . Hence, we estimate the absorption coefficient as written in Eq. 8.

**Estimation of  $\mu'_s$ :** While  $\mu_a$  can be estimated because absorption dominates the intensity fall-off for sufficiently large  $t$ , an analytical expression of  $\mu'_s$  in terms of the measurement is challenging. We numerically estimate  $\mu'_s$  with gradient descent. As shown in Eq. 4 and Eq. 5, the forward model is fairly complex. Our work uses recent advancements in auto-differentiation to calculate the gradient of the objective function (Eq. 6) with respect to  $\mu'_s$ . Automatic differentiation efficiently and accurately computes the derivative of functions from the forward model. It has been exploited for robust design optimization<sup>32</sup> computational fluid dynamics<sup>33</sup>, and has recently gained significant interest from machine learning community<sup>34</sup>. In imaging, automatic differentiation has been used in DOT with more complex forward model<sup>35,36</sup>, fluorescent lifetime imaging<sup>37</sup>. We use JAX<sup>38</sup> to implement the forward model in Eq. 4 and compute the gradient with respect to  $\mu'_s$ , and RMSProp as the optimizer<sup>39</sup>.

**Estimation of the target:** Given  $\mu'_s$  and  $\mu_a$ , the measurement can be computed by Eq. 4. This model can be further simplified as

$$\mathbf{b} = \mathbf{A}\mathbf{v}, \quad (9)$$

where  $\mathbf{b}$  and  $\mathbf{v}$  denote the vectorized 3D measurement  $m(x, y, t)$  and 2D target  $T(x, y)$  respectively.  $\mathbf{A}$  represents the mapping between the measurement target, and can be obtained by computing the expected measurement for each pixel of the target. For example,  $i$ th column of  $\mathbf{A}$  is the expected measurement for the case  $\mathbf{v}_i = 1$ , and given as

$$\mathbf{A}_i = \text{vec} \left( [\{I(x, y, t) * K_1(x, y, t; D, d_1)\} \odot T_i(x, y)] * K_2(x, y, t, D, d_2) \right), \quad (10)$$

where  $T_i(x, y)$  is 1 for the  $i$ th pixel and 0 for all the other pixels.  $\text{vec}(\cdot)$  denotes an operator that vectorizes 3D matrix into a normalized column vector. Eq. 9 is ill-posed because  $\mathbf{A}$  is a blurring operator. Therefore, we solve this problem with l1 and total variation regularizer  $\Gamma(\mathbf{v}) := \lambda_1 \|\mathbf{v}\|_1 + \lambda_2 \|\nabla \mathbf{v}\|_1$  to incorporate the priors of the mask.

$$\hat{\mathbf{v}} = \arg \min_{\mathbf{v}} \frac{1}{2} \|\mathbf{b} - \mathbf{A}\mathbf{v}\|^2 + \Gamma(\mathbf{v}). \quad (11)$$

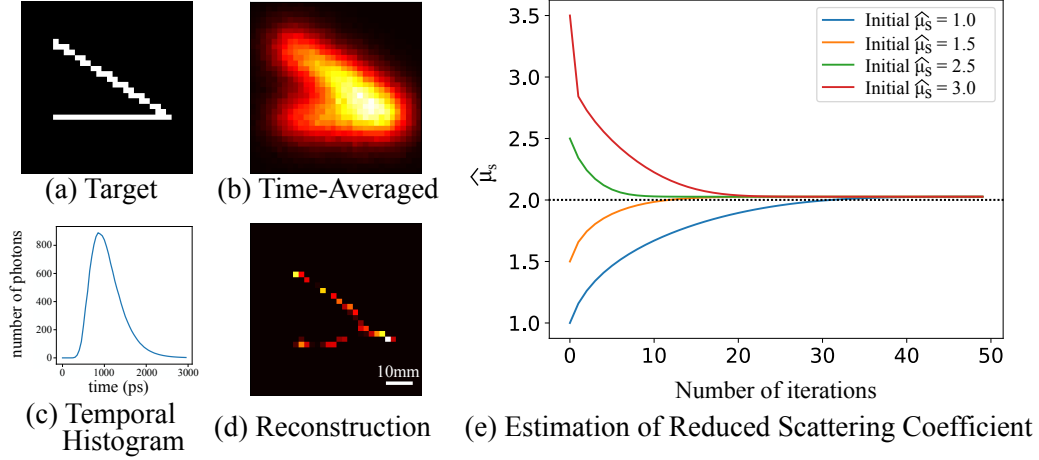


**Figure 4. Reconstruction results on the measurement simulated by Monte Carlo renderer.** (a) A Wedge-shaped target was used for rendering. (b) (c) The measurement is blurred in space and time due to scattering. (d) (e) Our technique recovers the target and the optical property of the scattering media. (e) Different initialization of the reduced scattering media converges close to the ground truth.

We use the alternating direction method of multipliers (ADMM)<sup>40</sup> to solve this minimization problem. The iterative steps of ADMM are summarized in Alg. 3.  $\mathbf{G}$  in the algorithm can be written as

$$\mathbf{G} = \begin{bmatrix} \mathbf{I} \\ \frac{\lambda_2}{\lambda_1} \mathbf{D}_x \\ \frac{\lambda_2}{\lambda_1} \mathbf{D}_y \end{bmatrix}, \quad (12)$$

where  $\mathbf{D}_x, \mathbf{D}_y$  are matrices that compute the gradient of the target in x and y directions, respectively.

While we use l1 sparsity prior to our target, our formulation could extend to types of common priors such as total-variation or sparsity over the discrete some bases (e.g., discrete cosine transform). When such priors are not available, Tikhonov (l2) regularization can be used (See Supplemental Material).

## Experimental Demonstration

We demonstrate our technique with both simulated and experimental data.

**Simulation:** We use a Monte Carlo renderer to simulate the time-of-flight measurements in our setup and validate our estimation of optical properties and the target. The simulated measurement does not contain any sensor noise, such as dark noise. The scattering coefficient, anisotropy, and absorption coefficient of the simulated phantom were  $20.0 \text{ mm}^{-1}$ , 0.9, and  $0.01 \text{ mm}^{-1}$ . The reduced scattering coefficient is  $2.0 \text{ mm}^{-1}$ . Fig. 4 shows the recovered target and reduced scattering coefficient for the first 50 iterations of  $\mu_s$  estimation. The estimated reduced scattering coefficient and the absorption coefficient was  $2.04 \text{ mm}^{-1}$  and  $0.011 \text{ mm}^{-1}$ . Fig. 4 shows that different initialization converges close to the ground truth.

**Experiment:** Fig. 3 illustrates the experimental setup. Fig. 5 shows the reconstruction results in 32 by 32 resolution with a pixel size of 2 mm, compared with time-averaged and ballistic-photon imaging. We integrated 2D frames with respect time for the time-averaged frame, which is equivalent to an image taken without the temporal resolution. We extract first photons above the noise level for each pixel to generate a ballistic frame (See Supplemental Material for the video of the measurements). The time-averaged frame shows blur due to the scattering. The ballistic frame is noisy because the number of ballistic photons is small. Our method successfully recovers the shape of the 2D target. The estimated reduced scattering and absorption coefficient are  $2.45 \text{ mm}^{-1}$  and  $0.0082 \text{ mm}^{-1}$  for "A" target, and  $2.39 \text{ mm}^{-1}$  and  $0.0088 \text{ mm}^{-1}$  for the "wedge" target.

Fig. 6 shows reconstruction results for different acquisition time. Our method is robust even when the SNR of the measurement is so low that the time-averaged and ballistic frames are noisy. Our technique reconstructed the "A" target with 150 ms exposure time. This shows the benefit of our simple optical setup. Fast acquisition is challenging with traditional DOT, which requires raster scanning of the illumination source. The accuracy of the estimation of the optical properties decreases as the acquisition time decreases. For example, for the acquisition time of 50ms, the estimated reduced scattering coefficient and absorption coefficient are  $2.04 \text{ mm}^{-1}$  and  $0.0031 \text{ mm}^{-1}$ . This is due to the estimation of the absorption coefficient from the

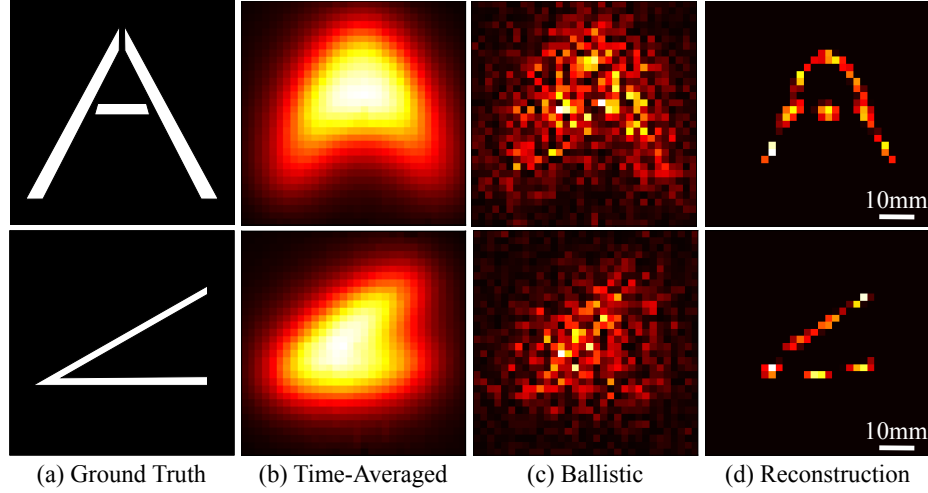


**Figure 5. Reconstruction results on the measurement from an experiment with 2D targets.** (a) Ground Truth. (b) Measurement integrated over time. (c) A frame with first arriving photons are captured. (d) Reconstruction.

noisy temporal histogram from a small number of photons. However, as shown in Fig. 7 (a)–(e), the estimated blur kernels  $K(x, y, t; D, d)$  for different acquisition times are still similar to the ground truth. Fig. 7 (f) plots the normalized intensity over time. The estimated kernel roughly follows the ground truth blur kernel, which we generated from the estimate of the optical properties with phantoms with no target.

## Discussion

**Reconstruction Complexity:** In this paper, we demonstrated the calibration-free reconstruction of a 2D mask in a scattering media. Our technique extends the limitations of previous works in complexity<sup>29</sup> or ease of use without calibration<sup>27</sup>. However, our technique still requires prior knowledge of the target depth, and many practical scenarios require reconstruction with more complexity, such as 3D reconstructions. The framework of our method to simultaneously estimate optical parameters and target with the auto-differential forward model can be extended to further complex scenes in future works.

**Resolution:** We used 2D targets that consist of two 2 mm by 10 mm bars that are 5 mm, 10 mm, 15 mm away from each other to evaluate the resolution of our system. Figure 8 shows the 1D reconstruction of the targets. This illustrates the resolution of our method for the same scattering media described in the experimental demonstration as compared to time-averaged and ballistic photon imaging. The resolution of imaging is determined by the blur due to the scattering media. The illustrated resolution should be worse as the scattering coefficient or the thickness of the phantom increase. Traditional DOT places illumination sources and detectors at different locations to capture more information for better reconstruction quality. In contrast, the goal of our technique is to improve the practicality of the imaging system.

**Need for Time-of-Flight Measurement:** Time-of-flight information plays an important role in the estimation of the diffusion coefficient. Our algorithm initializes an estimation of the target with the time-averaged frame. Without the time of flight, the estimation of the blur kernels  $K_1(x, y, t; D, d_1)$  and  $K_2(x, y, t; D, d_2)$  becomes an impulse response as the estimate becomes equivalent to the measurement.

**The Use of Diffusion Approximation and Linear Model:** While the linear model provides an approximation to RTE, the accuracy of the reconstruction is limited. Furthermore, the linear model may introduce an error because it does not model photon's random walk from the second phantom back to the first phantom across the target plane. Therefore, Monte Carlo-based reconstruction should produce better reconstruction result<sup>28</sup>. However, such a method requires many iterations of Monte-Carlo rendering. In contrast, diffusion-approximation-based reconstruction is more computationally efficient. In practice, our method can be used for the initialization of the Monte Carlo-based approach for faster convergence.

**Conclusion:** We propose a novel algorithm to reconstruct a mask in dense, scattering media with unknown optical properties using the auto-differential diffusion approximation model. We hope that our approach inspires more practical imaging through scattering media without extensive calibrations for biomedical and remote sensing applications. While our work reconstructs only 2D imaging, the implementation of auto-differential framework can be extended into 3D setting.

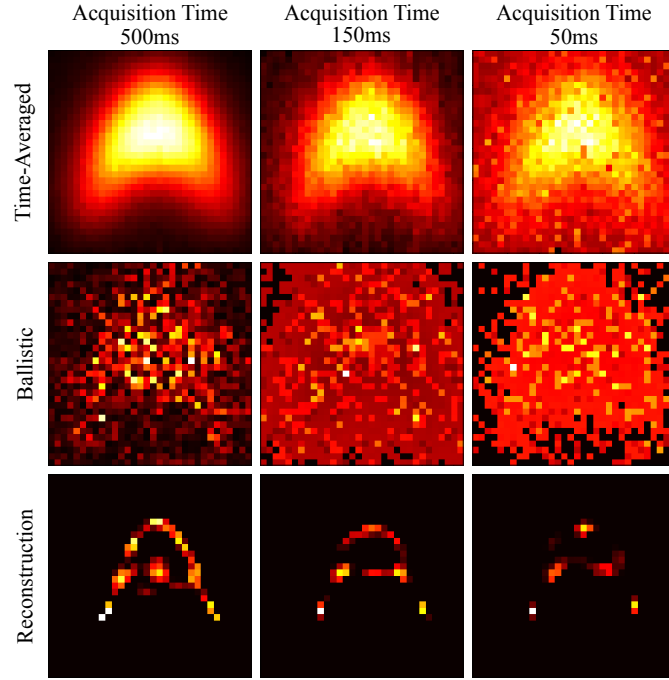


**Figure 6. Reconstruction with different acquisition times.** Our technique recovers the target with 150 ms acquisition time, showing the benefit of simple imaging setup with a single-shot capability.

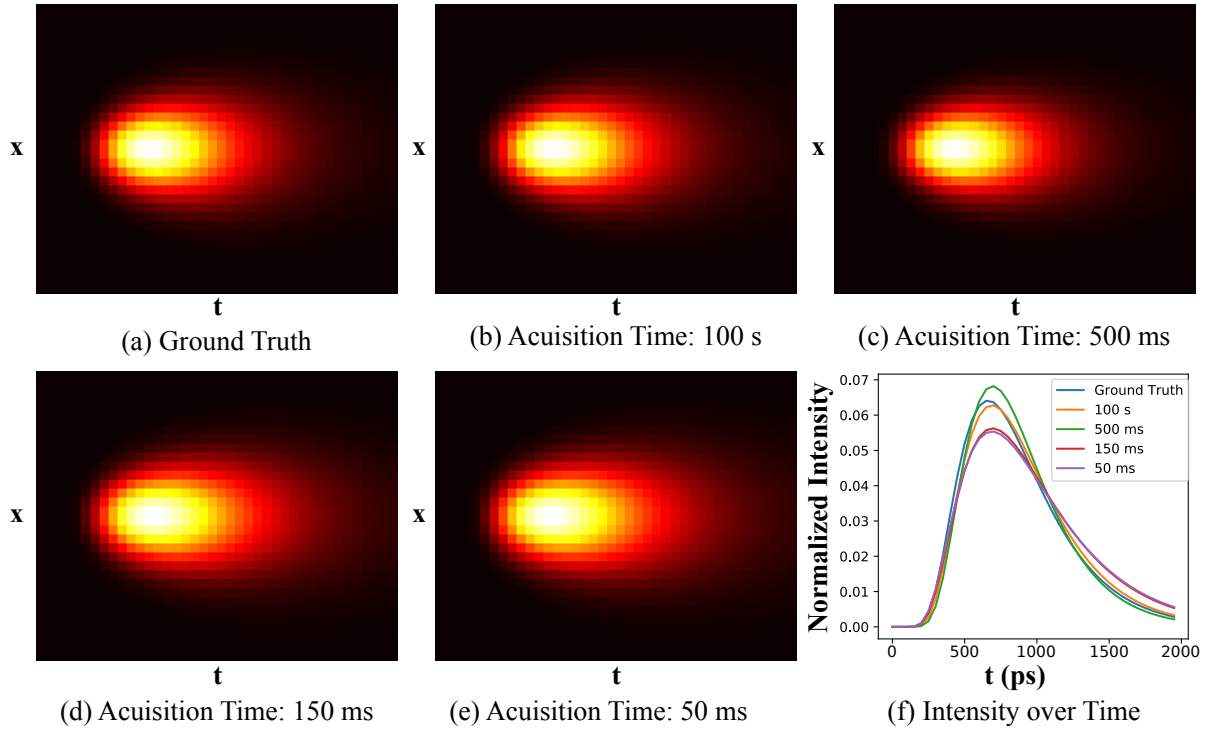


**Figure 7. Estimated blur kernels for measurements with different acquisition times.** The accuracy of the optical properties becomes worse with noise due to a shorter acquisition time. However, our technique is still able to estimate a blur kernel, which is close to the ground truth. (a)–(e) shows the  $x$ - $t$  plot of the intensity, and (f) shows the plot of normalized intensity over time for the estimates of the blur kernel with different acquisition times.



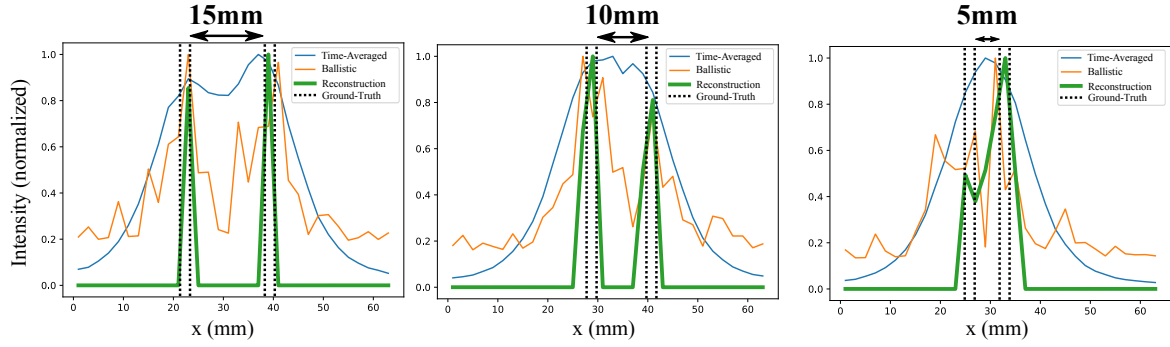


**Figure 8. Reconstruction of bars separated by 15 mm, 10 mm, 5 mm space to evaluate the resolution of our methods compared to time-averaged and ballistic reconstruction.** Time-averaged reconstruction suffers from blur due to scattering, and ballistic reconstruction suffers from low SNR. Our method resolves two points separated by 15mm and 10mm.

## Methods

**Optical setup:** Fig. 3 describes the optical setup. The SPAD array is focused on the surface of the tissue phantom, and one pixel corresponds to a 2 mm square patch on the surface. The illumination source is a SuperK super-continuum laser, where white light is filtered at 628 nm with acousto-optic tunable filters followed by a 50-degree circle diffuser (ThorLab, ED1-C50-MD), which was placed 6.4cm away from the phantom. The instrument response has roughly 150 ps full-width-half-max (FWHM). Each measurement is 32 x 32 x 70 tensor with a 50ps time bin. Exposure time is 0.5 ms for each frame of the SPAD array, and we measure 200000 frames for the complete measurement. The total acquisition time to generate reconstruction in Fig. 5 is 100 seconds. The biomimetic phantom consists of epoxy resin (East Coast Resin) as a base and  $\text{TiO}_2$  powder (Pure Organic Ingredients) as a scattering agent<sup>41</sup>. The refractive index of the media is 1.4<sup>41</sup> and both phantoms are 13 mm thick. We measured the absorption coefficient of the phantom as  $0.080 \text{ mm}^{-1}$  using Eq. 8 and the reduced scattering coefficient as  $2.32 \text{ mm}^{-1}$  by fitting the measurement with Eq. 5. For simulated measurement, we use the same parameters for the detector, and the illumination source was placed 10 cm away from the phantom. Reconstruction was performed on a 32 x 32 x 60 3D x-y-t measurement with a 50 ps time bin.

**Algorithm parameters:** All the reconstruction on experimental data was performed with  $\rho = 1$ ,  $\lambda_1 = 8 \times 10^{-4}$ , and  $\lambda_2 = 10^{-3}\lambda_1$ . The update of  $\mu'_s$  was performed with a step size of  $5 \times 10^{-2}$ , and terminated after a certain number of iterations or the change is less than 0.01%. Each  $\mu_s$  and  $T(x, y)$  has 300 and 50 iterations, alternated three times. The initial estimation of the reduced scattering coefficient was  $1.5 \text{ mm}^{-1}$  for all of our reconstruction. We used the time-averaged frame as the initialization of the target estimate. The reconstruction on simulated data was performed with  $\rho = 1$ ,  $\lambda_1 = 1 \times 10^{-4}$ , and  $\lambda_2 = 10^{-3}\lambda_1$ . Each  $\mu_s$  and  $T(x, y)$  has 300 and 50 iterations, alternated three times. We used larger  $\lambda_1$  for the experimental data because of higher noise level.

## References

1. Huang, D. *et al.* Optical coherence tomography. *Science* **254**, 1178 (1991).
2. Webb, R. H. Confocal optical microscopy. *Reports on Prog. Phys.* **59**, 427 (1996).
3. Helmchen, F. & Denk, W. Deep tissue two-photon microscopy. *Nat. Methods* **2**, 932–940 (2005).
4. Wang, L., Liu, Y., Ho, P. P. & Alfano, R. R. Ballistic imaging in biomedical samples using picosecond optical kerr gates. In *Conference on Lasers and Electro-Optics*, CTuH4 (Optical Society of America, 1991).
5. Naik, N., Barsi, C., Velten, A. & Raskar, R. Estimating wide-angle, spatially varying reflectance using time-resolved inversion of backscattered light. *J. Opt. Soc. Am. A* **31**, 957–963, DOI: [10.1364/JOSAA.31.000957](https://doi.org/10.1364/JOSAA.31.000957) (2014).
6. Satat, G. *et al.* Locating and classifying fluorescent tags behind turbid layers using time-resolved inversion. *Nat. communications* **6**, 6796, DOI: [10.1038/ncomms7796](https://doi.org/10.1038/ncomms7796) (2015).
7. Wang, J. J., Bartels, J. R., Whittaker, W., Sankaranarayanan, A. C. & Narasimhan, S. G. Programmable triangulation light curtains. In *ECCV* (2018).
8. Achar, S., Bartels, J. R., Whittaker, W. L. R., Kutulakos, K. N. & Narasimhan, S. G. Epipolar time-of-flight imaging. *ACM Trans. Graph.* **36**, 37:1–37:8, DOI: [10.1145/3072959.3073686](https://doi.org/10.1145/3072959.3073686) (2017).



9. O'Toole, M., Raskar, R. & Kutulakos, K. N. Primal-dual coding to probe light transport. *ACM Trans. Graph.* **31**, 39:1–39:11, DOI: [10.1145/2185520.2185535](https://doi.org/10.1145/2185520.2185535) (2012).
10. Bertolotti, J. *et al.* Non-invasive imaging through opaque scattering layers. *Nature* **491**, 232–4, DOI: [10.1038/nature11578](https://doi.org/10.1038/nature11578) (2012).
11. Katz, O., Heidmann, P., Fink, M. & Gigan, S. Non-invasive real-time imaging through scattering layers and around corners via speckle correlations. *Nat. Photonics* **8**, DOI: [10.1038/nphoton.2014.189](https://doi.org/10.1038/nphoton.2014.189) (2014).
12. Freund, I., Rosenbluh, M. & Feng, S. Memory effects in propagation of optical waves through disordered media. *Phys. Rev. Lett.* **61**, 2328–2331, DOI: [10.1103/PhysRevLett.61.2328](https://doi.org/10.1103/PhysRevLett.61.2328) (1988).
13. Drémeau, A. *et al.* Reference-less measurement of the transmission matrix of a highly scattering material using a dmd and phase retrieval techniques. *Opt. Express* **23**, 11898–11911 (2015).
14. Metzler, C. A. *et al.* Coherent inverse scattering via transmission matrices: Efficient phase retrieval algorithms and a public dataset. In *2017 IEEE International Conference on Computational Photography (ICCP)*, 1–16 (2017).
15. Wang, X. *et al.* Noninvasive laser-induced photoacoustic tomography for structural and functional in vivo imaging of the brain. *Nat. Biotechnol.* **21** (2003).
16. Wang, L. V. Tutorial on photoacoustic microscopy and computed tomography. *IEEE J. Sel. Top. Quantum Electron.* **14**, 171–179, DOI: [10.1109/JSTQE.2007.913398](https://doi.org/10.1109/JSTQE.2007.913398) (2008).
17. Maslov, K., Stoica, G. & Wang, L. V. In vivo dark-field reflection-mode photoacoustic microscopy. *Opt. Lett.* **30**, 625–627, DOI: [10.1364/OL.30.000625](https://doi.org/10.1364/OL.30.000625) (2005).
18. Gibson, A., Hebden, J. & Arridge, S. Recent advances in diffuse optical imaging. *Phys. medicine biology* **50**, R1–43, DOI: [10.1088/0031-9155/50/4/R01](https://doi.org/10.1088/0031-9155/50/4/R01) (2005).
19. Boas, D. A. *et al.* Imaging the body with diffuse optical tomography. *IEEE Signal Process. Mag.* **18**, 57–75, DOI: [10.1109/79.962278](https://doi.org/10.1109/79.962278) (2001).
20. Corlu, A. *et al.* Three-dimensional in vivo fluorescence diffuse optical tomography of breast cancer in humans. *Opt. Express* **15**, 6696–6716, DOI: [10.1364/OE.15.006696](https://doi.org/10.1364/OE.15.006696) (2007).
21. Velten, A. *et al.* Recovering three-dimensional shape around a corner using ultrafast time-of-flight imaging. *Nat. communications* **3**, 745 (2012).
22. Satat, G., Tancik, M. & Raskar, R. Towards photography through realistic fog. In *2018 IEEE International Conference on Computational Photography (ICCP)*, 1–10, DOI: [10.1109/ICCPHOT.2018.8368463](https://doi.org/10.1109/ICCPHOT.2018.8368463) (2018).
23. Kadambi, A. *et al.* Coded time of flight cameras: sparse deconvolution to address multipath interference and recover time profiles. *ACM Transactions on Graph. (TOG)* **32**, 167 (2013).
24. Heshmat, B., Tancik, M., Satat, G. & Raskar, R. Photography optics in the time dimension. *Nat. Photonics* **12**, DOI: [10.1038/s41566-018-0234-0](https://doi.org/10.1038/s41566-018-0234-0) (2018).
25. Kumar, A. T. N., Raymond, S. B., Boverman, G., Boas, D. A. & Bacskaï, B. J. Time resolved fluorescence tomography of turbid media based on lifetime contrast. *Opt. Express* **14**, 12255–12270, DOI: [10.1364/OE.14.012255](https://doi.org/10.1364/OE.14.012255) (2006).
26. Pifferi, A. *et al.* New frontiers in time-domain diffuse optics, a review. *J. Biomed. Opt.* **21**, 091310, DOI: [10.1117/1.JBO.21.9.091310](https://doi.org/10.1117/1.JBO.21.9.091310) (2016).
27. Lyons, A. *et al.* Computational time-of-flight diffuse optical tomography. *Nat. Photonics* **13**, DOI: [10.1038/s41566-019-0439-x](https://doi.org/10.1038/s41566-019-0439-x) (2019).
28. Gkioulekas, I., Levin, A. & Zickler, T. E. An evaluation of computational imaging techniques for heterogeneous inverse scattering. In *ECCV* (2016).
29. Satat, G., Heshmat, B., Raviv, D. & Raskar, R. All photons imaging through volumetric scattering. *Sci. Reports* **6**, 33946, DOI: [10.1038/srep33946](https://doi.org/10.1038/srep33946) (2016).
30. Patterson, M. S., Chance, B. & Wilson, B. C. Time resolved reflectance and transmittance for the noninvasive measurement of tissue optical properties. *Appl. Opt.* **28**, 2331–2336, DOI: [10.1364/AO.28.002331](https://doi.org/10.1364/AO.28.002331) (1989).
31. Chance, B. *et al.* Time-resolved spectroscopy of hemoglobin and myoglobin in resting and ischemic muscle. *Anal. biochemistry* **174**, 698–707 (1988).
32. Renaud, J. Automatic differentiation in robust optimization. *AIAA journal* **35**, 1072–1079 (1997).

33. Bischof, C. *et al.* Automatic differentiation of advanced cfd codes for multidisciplinary design. *J. on Comput. Syst. Eng.* **3**, 625–637 (1992).
34. Baydin, A. G., Pearlmutter, B. A., Radul, A. A. & Siskind, J. M. Automatic differentiation in machine learning: A survey. *J. Mach. Learn. Res.* **18**, 5595–5637 (2017).
35. Arridge, S. R. & Schweiger, M. A gradient-based optimisation scheme for optical tomography. *Opt. Express* **2**, 213–226, DOI: [10.1364/OE.2.000213](https://doi.org/10.1364/OE.2.000213) (1998).
36. D. Klose, A. & Hielscher, A. Optical tomography using the time-independent equation of radiative transfer-part 2: Inverse model. *J. Quant. Spectrosc. Radiat. Transf.* **72**, 715–732, DOI: [10.1016/S0022-4073\(01\)00151-0](https://doi.org/10.1016/S0022-4073(01)00151-0) (2002).
37. Roy, R. & Sevick-Muraca, E. M. Truncated newton’s optimization scheme for absorption and fluorescence optical tomography: Part i theory and formulation. *Opt. Express* **4**, 353–371, DOI: [10.1364/OE.4.000353](https://doi.org/10.1364/OE.4.000353) (1999).
38. Johnson, M., Frostig, R., Maclaurin, D., & Leary., C. Jax: Autograd and xla (2018).
39. Hinton, G., Srivastava, N. & Swersky, K. Neural networks for machine learning lecture 6a overview of mini-batch gradient descent. .
40. Boyd, S., Parikh, N., Chu, E., Peleato, B. & Eckstein, J. Distributed optimization and statistical learning via the alternating direction method of multipliers. *Found. Trends Mach. Learn.* **3**, 1–122, DOI: [10.1561/22000000016](https://doi.org/10.1561/22000000016) (2011).
41. Diep, P. *et al.* Three-dimensional printed optical phantoms with customized absorption and scattering properties. *Biomed. Opt. Express* **6**, 4212–4220, DOI: [10.1364/BOE.6.004212](https://doi.org/10.1364/BOE.6.004212) (2015).

## Acknowledgments

We thank Ioannis Gkioulekas for useful discussions. We thank Prof. Mounji Bawendi, Nathan Klein and Collin Perkinson for their generous support of experimental hardware. Tomohiro Maeda and Ramesh Raskar are supported by Media Lab consortium funding and NSF Expeditions award IIS-1729931 and DARPA Reveal Program N00014-18-1-2894. Ankit Ranjan is supported by St John’s College, Oxford Special Grant Fund.

## Author Contributions

T.M. developed the method, performed experiments, and analyzed data. T.M and A.R designed the experiment. R.R. supervised the project. All authors contributed in preparing the manuscript.

## Competing interests

The authors declare no competing interests.